




## Ultra-broadband symmetrical acoustic coherent perfect absorbers designed by the causality principle

Caixing Fu <sup>1</sup>, Min Yang,<sup>2</sup> and Zhi Hong Hang <sup>1,3,\*</sup>

<sup>1</sup>*School of Physical Science and Technology and Collaborative Innovation Center of Suzhou Nano Science and Technology, Soochow University, Suzhou 215006, China*

<sup>2</sup>*Acoustic Metamaterials Group Ltd, Data Technology Hub, No. 5 Chun Cheong Street, Tseung Kwan O, Hong Kong, China*

<sup>3</sup>*Institute for Advanced Study and Provincial Key Lab of Thin Films, Soochow University, Suzhou 215006, China*

 (Received 9 May 2023; revised 20 September 2023; accepted 26 September 2023; published 7 November 2023)

We report a methodology to reach the symmetrical broadband coherent perfect absorption in an air tube whose reliability and feasibility are demonstrated experimentally. Through rigorous analytical calculations, we discover that the causality principle provides a minimal volume requirement based on absorption capability, while the idealistic coherent symmetrical perfect absorption cannot be achieved but can be approached within a finite volume. As a demonstration, a side-loaded near-perfect absorber is designed and realized working at a broad bandwidth from 300 to 5000 Hz without blocking the tube. The size of the absorber is also super-subwavelength, only 1% of the longest working wavelength. By experimentally measuring the absorption in both frequency and time domains, broadband and tunable near-perfect coherent absorption properties are demonstrated. In addition, we achieve the manipulation of sound waves in a ventilated tube by using sound pulses.

DOI: [10.1103/PhysRevResearch.5.L042020](https://doi.org/10.1103/PhysRevResearch.5.L042020)

Acoustic absorption is a traditional yet active topic since low-frequency broadband absorption in subwavelength remains challenging in many application scenarios, like controlling noise from ventilation systems [1]. In recent years, researchers have made great efforts in the study of acoustic metamaterials [2–10], which can create intriguing properties that cannot be found in nature, such as negative refraction and superlensing [2–5], acoustic cloaking [6–8], and one-way transmittance [9,10]. These resonance-based novel properties of metamaterials also shed new light on the age-old topic of acoustic absorption and noise reduction in ducts [11–17]. Ingeniously designed resonances can increase the energy density inside materials and realize a series of efficient subwavelength acoustic absorbers [18–27]. By integrating multiple quarter-wavelength resonators, Yang *et al.* showed that the original narrowband metamaterial absorption could be further extended to broadband and approached the limit allowed by the law of causality [26]. In this paper, we will combine this broadband metamaterial technology [28–31] with coherent perfect absorption (CPA) and control the absorption performance in broadband by two coherently incident sounds. Proposed in optics [32–37] and then demonstrated in microwaves [38], CPA attracts a wide range of research interests, including heat transfer [39] and acoustic waves [40–45]. Based on different parity features, CPA is divided into symmetric and antisymmetric types [41]. Perfect absorption can

only be achieved if the absorber is symmetrically matched to the incident waves, which makes it possible to use a wave to control the absorption of another wave [43]. We take an absorber that satisfies the broadband symmetric CPA condition as an example. By adjusting the amplitude and phase of the control wave relative to the incident wave, the system absorption can change from 100% in the case of the two waves of symmetry (the same amplitude and phase) to 0% when the two waves are antisymmetric (the same amplitude but a phase difference of  $\pi$ ).

Although broadband CPA has been realized by thin metal films [45], the sound transmission path must be partially blocked so it significantly increases the air flow resistance. Here, we start from the causality constraint on the absorption efficiency and bandwidth of symmetric CPA and find that the idealistic broadband acoustic coherent perfect absorption (BACPA) does not exist in a finite volume. However, we can still make the most of the limited volume to approach the BACPA. As shown in Fig. 1, quarter-wavelength resonant channels, also known as Fabry-Perot (FP) channels, are loaded on the side wall of an air tube to achieve a symmetrical BACPA effect with two coherent waves. The opening of FP channels along the direction of sound propagation is ultra-subwavelength (1% of the wavelength of the lowest target frequency), and its side-loaded nature ensures that the tube is unobstructed. The broadband near-perfect absorption is experimentally demonstrated in frequency and time domains, which agrees well with theoretical predictions. Furthermore, in a ventilated tube, we used a sound pulse to successfully control the absorption efficiency of another pulse by adjusting its relative phase and amplitude.

We can simplify the physics discussion in the air tube system into a one-dimensional problem due to the subwavelength dimension of the tube cross section [46]. Therefore, for CPA,

\*zhhang@suda.edu.cn

Published by the American Physical Society under the terms of the [Creative Commons Attribution 4.0 International](https://creativecommons.org/licenses/by/4.0/) license. Further distribution of this work must maintain attribution to the author(s) and the published article's title, journal citation, and DOI.

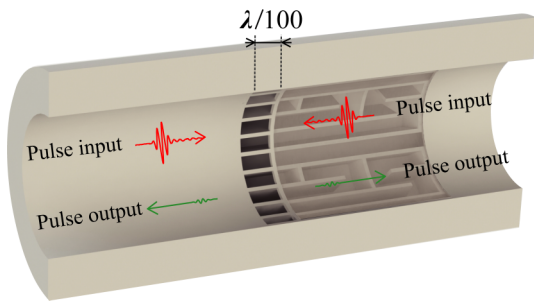


FIG. 1. Schematic of a broadband near-perfect absorber under coherent inputs. The transparent structure shows the folded FP channels on the side wall of the tube, and their opening apertures are ultra-subwavelength, while the rest can be considered part of the tube. Besides, the side-loaded design ensures free ventilation in the tube.

the two incident sound waves can be treated as plane waves impinging on a sample from forward and backward directions. The wave equation is given as  $t(r)p_i^L + r(t)p_i^R = p_o^{R(L)}$ , where  $t(r)$  is the complex transmission (reflection) coefficient,  $p_i^{R(L)}$  and  $p_o^{R(L)}$  are the far-field components of the complex pressure field with reference to the middle plane of the sample in the right ( $R$ ) and left ( $L$ ) directions denoted by the superscripts. The subscripts  $i$  and  $o$  stand for the input and output waves. For symmetrical inputs, the condition to realize the CPA effect requires  $t = -r$  under a single-sided incidence, and resonators, such as membrane-type resonators, Helmholtz resonators, etc., are good candidates for this goal [41,43]. In this manuscript, we choose FP channels and load them on the air tube's side wall to ensure the tube is unblocked. As the side-loaded FP channels suck and push the air simultaneously in the axial direction along the waveguide, a symmetrical response but not an antisymmetrical response is generated ( $t - r - 1 = 0$ ). The complex transmission and reflection coefficients are then solved as

$$t = -r = 0.5, \quad (1)$$

for one-sided incident waves when the CPA effect is reached. Based on the continuity of sound pressure and volume velocity at the resonator with a subwavelength scale, the target surface impedance of side-loaded FP channels can be retrieved as  $Z_b = \rho_0 c_0 / (2S_0)$ , where  $\rho_0$  and  $c_0$  represent the density and sound speed of air, and  $S_0$  stands for the cross-sectional area of the air tube.

Thus, we assume that the target surface impedance of side-loaded FP channels satisfies  $Z_b = \rho_0 c_0 / (2S_0)$  within the customized frequency range of  $(\omega_1, \omega_N)$  for coherent perfect absorption, and its reciprocal is zero elsewhere. However, according to the Kramers-Kronig relationship, the above real-valued surface impedance is necessarily accompanied by an unavoidable imaginary part, so perfect absorption cannot be achieved, and the corresponding scattering coefficient is given as

$$S(\lambda) = \frac{\pi + 2i \tanh^{-1} \lambda / \lambda_1 - 2i \tanh^{-1} \lambda / \lambda_N}{\pi - 2i \tanh^{-1} \lambda / \lambda_1 + 2i \tanh^{-1} \lambda / \lambda_N}, \quad (2)$$

where  $\lambda_{1(N)} = 2\pi c_0 / \omega_{1(N)}$  denotes the wavelength at the lower (upper) bound of the designed frequency band  $\omega_1(\omega_N)$ .

As shown in Ref. [26], such a gap between Eq. (2) and perfect absorption comes from the finite volume of the system. We apply similar analyses to the specific scenario of CPA and get the following relationship:

$$V_{b\_min} = \frac{S_0 B_{eff}}{\pi^2 B_0} \left| \int_0^\infty \ln |S(\lambda)| d\lambda \right| \leq V_b. \quad (3)$$

Here,  $V_b$  is the volume of the side-loaded resonators,  $B_{eff}$  is their effective bulk modulus, and  $B_0$  is the bulk modulus of air. The detailed derivations can be found in the Supplemental Material [47]. According to Eq. (3), the idealistic BACPA with  $S(\lambda) = 0$  is impossible for a finite  $V_b$  since the integral will diverge, and any imperfect spectrum [ $S(\lambda) \neq 0$ ] shall correspond to a minimal volume  $V_{b\_min}$  for the side-loaded resonators. Therefore, instead of pursuing the idealistic BACPA, which is impossible in reality, we will try to design an absorber that satisfies the Kramers-Kronig relations to approach the idealistic one. By substituting Eq. (2) into Eq. (3), the minimal volume of the BACPA design is obtained as

$$V_{b\_min} = \frac{2S_0 B_{eff}}{\pi^2 B_0} (\lambda_1 - \lambda_N). \quad (4)$$

As mentioned above, side-loaded FP channels are used to construct the symmetrical BACPA. Each one has the same cross-sectional area, and their surface impedance is expressed in Lorentzian form as [26]

$$Z_b = \frac{iNz_0}{\omega S_b} \left[ \sum_{n=1}^N \sum_{m=0}^{\infty} \frac{4\Omega_n / \pi}{(2m+1)^2 \Omega_n^2 - \omega^2 - i\beta_n \omega} \right]^{-1}, \quad (5)$$

where  $z_0 = \rho_0 c_0$  is the specific acoustic impedance of air,  $S_b$  is the total cross-sectional area of FP channels with numbers of  $N$ ,  $\Omega_n$  indicates the first-order resonant frequency of the  $n$ th FP channel,  $\beta_n$  represents its damping coefficient, and the terms with  $m > 0$  denote higher-order resonances. The higher-order resonances present an adjustment to the target surface impedance, so a more precise scattering coefficient and a revised minimal volume are described in Sec. II of the Supplemental Material [47]. To realize the BACPA design, our task is to properly optimize the number of FP channels ( $N$ ) and determine the length of each FP channel to match Eq. (5) with the target impedance. Owing to the interference of higher orders arising from first-order resonances, the first-order resonant frequency of each FP channel should be expressed by a piecewise function. In each frequency range, i.e., for  $\Omega \in [(2i-1)\Omega_1, (2i+1)\Omega_1]$ , the first-order resonant frequency is given by  $\Omega_n = (2i-1)\Omega_1 e^{2\phi(\bar{n}-\bar{n}_i)\tilde{Z}_i/Z_0}$ . Here, index  $i$  starts from 1;  $\Omega_1$  is the lower bound frequency ( $\omega_1$ ) of the BACPA design;  $\phi$  is the area ratio defined by  $S_b/S_0$ ,  $Z_0 = \rho_0 c_0 / S_0$ ,  $\bar{n} = (n-1)/N$ ,  $\bar{n}_i = N_i/N$  with  $N_i$  is the total number of first-order modes below  $(2i-1)\Omega_1$ ; and  $\tilde{Z}_i$  is obtained from iterations based on a target surface impedance. Considering the upper bound frequency ( $\omega_N$ ), we can get the area ratio and have the frequency distribution of FP channels. The detailed methodology is described in the Supplemental Material [47]. Based on this method, we can achieve the symmetrical BACPA design for any given frequency range.

In practice, we took the operating frequency range from 300 to 5000 Hz as an example and used 25 FP channels with various lengths to verify the above scheme. The first-order

TABLE I. The first-order resonant frequency of each FP channel.

$n$	1	2	3	4	5	6	7	8
$\Omega_n/2\pi$	300	323	347	374	402	433	465	500
9	10	11	12	13	14	15	16	17
538	579	623	670	721	776	835	898	1001
18	19	20	21	22	23	24	25	
1117	1246	1391	1574	1841	2177	2729	3468	

resonant frequency of each FP channel is given in Table I with its corresponding length as  $l_n = \pi c_0/(2\Omega_n)$ . In addition, the cross-sectional area [ $a'$  shown in Fig. 2(b)] of each FP channel is given as  $1.83S_0/25$ . Thus the actual volume (wall thickness excluded) occupied by 25 FP channels is  $0.24S_0$ , counting from  $\sum_1^{25} l_n a'$ , whereas the minimal volume dictated by the causality constraint is  $0.23S_0$ . Two very close values are seen, which demonstrates the reliability of our design strategy for obtaining the minimal volume. Moreover, the volume can further approach the causality limit by raising the number of FP channels—at the cost of complex structure, though.

Since we have all the structural parameters to construct the BACPA sample, the last task is to load these FP channels around the side wall of the air tube. As shown in Fig. 2(a), we place the opening ends of 25 FP channels around an air tube at the same  $x$ - $y$  plane and fold the long FP channels behind the short ones to obtain a compact structure with a 30 mm inner diameter (the same as that of the impedance tube), a 59 mm outer diameter, and a 133 mm length in the  $z$  direction. In this BACPA design, the opening only covers a length of 11.5 mm in the  $z$  direction, and the remaining can be considered part of the air tube. Figure 2(b) shows its  $x$ - $y$  plane sectional view. The orange area  $a'$  displays the fan-shaped cross section of one FP channel with an area of  $52 \text{ mm}^2$ , and the areas outlined in gray represent the structural wall. The whole structure was fabricated by a three-dimensional printer using photosensitive resin composites with an accuracy of 0.1 mm.

Experiments adopting an impedance tube method [21] were conducted to demonstrate the BACPA effect with the setup schematically shown in Fig. 3(a). Two loudspeakers mounted at both ends provide incident waves with phases and amplitudes being respectively controlled by a two-channel signal generator (Tektronix AFC3022C), and the BACPA sample is sandwiched in the middle of the tube to ensure

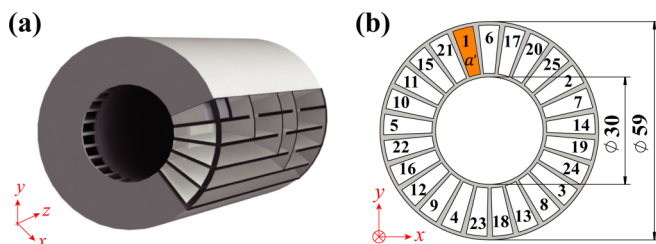


FIG. 2. (a) Schematic diagram of the BACPA sample. (b) The  $x$ - $y$  plane sectional view of the BACPA sample. The orange area indicates the cross-sectional area of one FP channel and the number labeled in each cross section represents the  $n$ th FP channel.

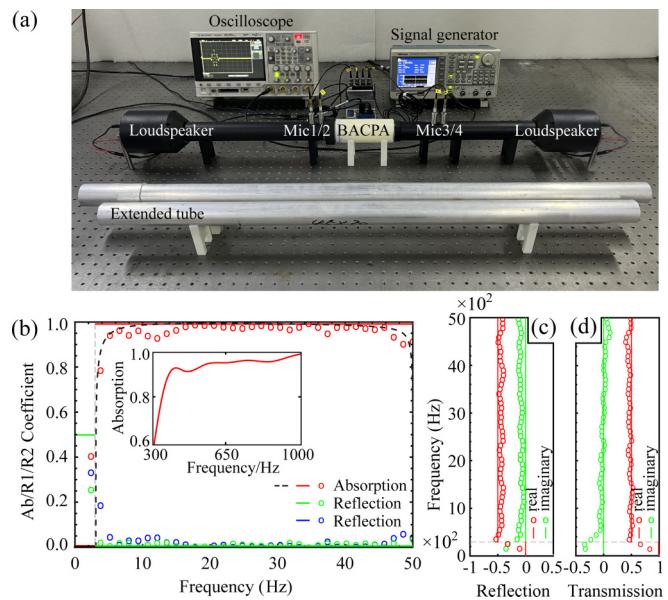


FIG. 3. Experimental demonstration for BACPA. (a) Schematic of the experimental setup. For two- and one-port input, four microphones attached at the surface of the impedance tube record the data of sound pressure with the NI9234, and the BACPA sample's absorption and scattering coefficients are then obtained as shown in (b) with two coherent inputs, and (c), (d) with one-port input. Solid curves represent theoretical results, and open circles stand for experimental data. Very good agreement is seen. Inset: zoomed-in plot of experimental absorption coefficient between 300 and 1000 Hz in (b).

an equal distance from its opening to two loudspeakers. When coherently incident from both sides, the absorption coefficient is given as  $A = 1 - R1 - R2$  with  $R1(2) = |p_o^{L(R)}|^2 / (|p_i^L|^2 + |p_i^R|^2)$  denoting the reflection intensity from the left (right) tube. Figure 3(b) shows its experimental results (open circles) of near-perfect absorption in the frequency range of 300 and 5000 Hz. The solid red curve represents the idealistic BACPA, while the dashed curve indicates the theoretical near-perfect absorption subject to causality constraints. By averaging the absorption coefficient from the dashed curve over the operating frequency range (300–5000 Hz), we get 99% absorption efficiency, which almost approaches the idealistic BACPA. Furthermore, as shown in Figs. 3(c) and 3(d), the scattering coefficients with a one-sided input wave were also experimentally measured (open circles), showing a good consistency with the theory (curves) indicated by Eq. (1). The slight differences between experiments and theory may result from sample processing and testing errors. Except for the opening area of the sample, the rest of the inner wall can be considered part of the tube, so we successfully realized an ultra-subwavelength ( $\lambda/100$ ) symmetrical BACPA compared to the lowest operating frequency of 300 Hz with a 1.14 m wavelength.

Moreover, the ultra-broadband absorption opens the way to extend the application of CPA to the pulsed signal in the time domain, which has industrial applications in active noise reduction. We choose two Gaussian beams of the same amplitude but different phases to visualize the phenomenon.



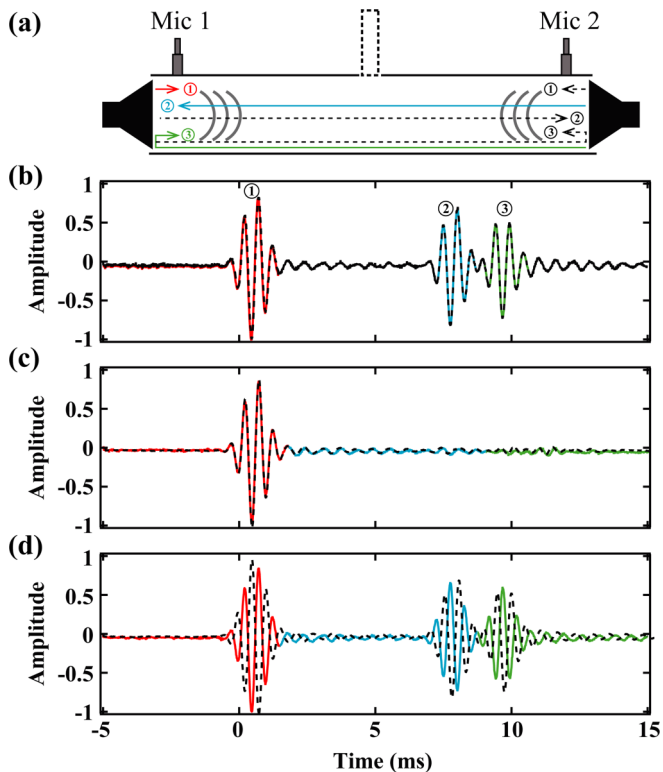


FIG. 4. The measurement of temporal signals. (a) Schematic of the experiment with two input waves. (b) Measured pulses at Mic 1 (solid lines) and Mic 2 (dashed lines) when the sample is absent. The first and second pulses are directly from loudspeakers, while the third comes from the reflection of a nearby loudspeaker. (c), (d) Measured pulses at Mic 1 (solid lines) and Mic 2 (dashed lines) when the sample is present. The amplitudes of the two inputs are the same, while its relative phase is  $0$  (c) and  $\pi$  (d).

We can anticipate that wave packets incident from the two tube ends with zero phase difference will be totally absorbed, while it will lead to a total scattering if their phase difference is  $\pi$ . In experiment, two extension tubes were additionally used to lengthen the left and right impedance tubes to distinguish adjacent pulse signals, and an oscilloscope (Agilent DSO-X3024A) was used to record signals [see Fig. 3(a)]. The experiment is schematically shown in Fig. 4(a) with two microphones placed 26 cm away from the left and right loudspeakers and three solid and dashed lines describing the propagation path of the first three pulse signals (labeled by ①, ②, ③) from microphones 1 and 2, respectively. Arrows represent the direction of sound waves. For reference, Fig. 4(b) presents the situation if the sample is absent and the output signals from both loudspeakers have the same amplitude and phase. Three wave packets arrive at Mic 1 and are visualized at different timepieces, with red, blue, and green lines corresponding to the pulse signals from path ①, ②, and ③, respectively. Furthermore, the first three wave packets arriving at Mic 2 (depicted by the black dashed lines) have the same characteristics as signals from Mic 1. The value of  $0$  ms on the abscissa represents the moment when the loudspeakers generate the signals. At the same time, the magnitude of each datum is normalized by the maximum value of the test signal.

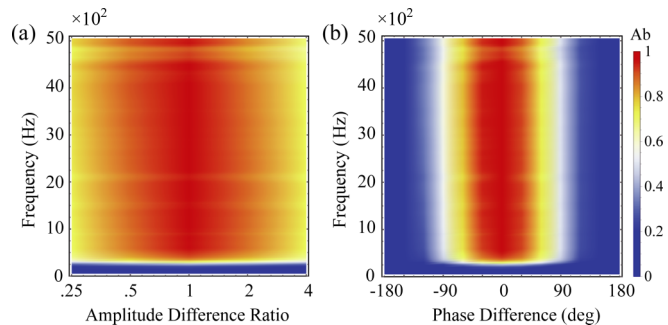


FIG. 5. Numerical simulation of two-port input with different acoustic incident conditions. (a) The relationship between the absorption efficiency and the relative amplitude of the two input waves. (b) Absorption efficiency as a function of the relative phase of the two inputs.

We here truncate the extra signals due to other reflections on the loudspeakers. The slight difference between the amplitude of the three signals comes from the intrinsic dissipation in the impedance tube. By tuning the phase difference of two pulses to  $\pi$ , the amplitudes of the three wave packets from Mic 1 and 2 are similar to those recorded in the in-phase case.

When sandwiching the sample at the midposition inside the two impedance tubes, we observe the same amplitude of the first wave packet in both Figs. 4(c) and 4(d) with the incident phase set as  $\theta = 0$  and  $\theta = \pi$ . However, the second and third wave packets are absent in Fig. 4(c), whereas they are detectable in Fig. 4(d) with almost the same amplitude as in Fig. 4(b). Therefore, we demonstrated the symmetrical BACPA in time domain experiments and effectively regulated its absorption efficiency. In addition, regarding pulses from both loudspeakers as noise and anti-noise sources, the noise can be completely eliminated by dynamically synchronizing the amplitude and phase of the noise-cancellation loudspeaker. Compared with the traditional active noise cancellation (ANC) based on reflection, this near-perfect absorbing device may have more benefits. Specifically, reflection-based ANC requires an antisource with the same moving direction, and its significant transmission loss is obtained at the cost of providing considerable reflections. Our technology demonstrated here needs two-port sources, and the absorption efficiency can be arbitrarily tuned, which is more beneficial in a coaxial loudspeaker system, widely used for car audio systems and omnidirectional loudspeakers. With two loudspeakers connected tail to tail (see Refs. [48,49], the interference from the rear radiating waves of both diaphragms can be near-perfectly canceled by mounting the BACPA design in the middle of the two mirrored coaxial diaphragms. As both loudspeakers have the same in-phase signal, no further active signal control is needed.

To further demonstrate the feasibility of using one wave to control the absorption of another wave, we used COMSOL MULTIPHYSICS to investigate the absorption efficiency as a function of the relative amplitude and phase. In simulations, we used the actual structural parameters to study two scenarios: keeping the same phase of the two input waves but adjusting for amplitude differences and the opposite case. As shown in Fig. 5(a), the absorption coefficient will only change

from 1 to 0.7 if a significant amplitude difference, with a ratio from 1 to 4, is applied. It indicates that the absorbing capacity of the design is insensitive to the amplitude differences when maintaining identical incident phases. However, in another scenario shown in Fig. 5(b), the absorption can change from unity to zero within all the designed frequencies by tuning the phase difference from 0 to  $\pi$ . Therefore, by adjusting the relative phase difference of the two inputs, we have successfully achieved arbitrary regulation of the absorption efficiency.

In summary, we have demonstrated that the idealistic BACPA cannot be achieved in a given volume. However, we can still use a minimal volume connected with the operating frequency bandwidth to approach it under the causality constraint. We raised a methodology to design the structure and experimentally verified its broadband near-perfect absorption in both frequency and time (by sound pulse) domains. The

tunability of the absorption efficiency was investigated by adjusting the relative phase and amplitude of the two input waves. Consequently, the absorption is found to be phase sensitive but not amplitude sensitive. This broadband near-perfect absorber with an ultra-subwavelength scale is useful for noise reduction in ventilated tubes. In addition, phase-sensitive absorption facilitates the manipulation of sound pulses, thereby allowing for active noise cancellation and wave control.

This work was supported by the National Key R&D Program of China (Grant No. 2022YFA1404400), the National Natural Science Foundation of China (Grant No. 12274315), and a Project Funded by the Priority Academic Program Development of Jiangsu Higher Education Institutions (PAPD). We thank Mengyao Xie, Yunfei Xu, and Songwen Xiao for their helpful discussions.

- 
- [1] M. Yang and P. Sheng, Sound absorption structures: From porous media to acoustic metamaterials, *Annu. Rev. Mater. Res.* **47**, 83 (2017).
- [2] S. H. Lee, C. M. Park, Y. M. Seo, S. G. Wang, and C. K. Kim, Composite acoustic medium with simultaneously negative density and modulus, *Phys. Rev. Lett.* **104**, 054301 (2010).
- [3] Z. Liang and J. Li, Extreme acoustic metamaterial by coiling up space, *Phys. Rev. Lett.* **108**, 114301 (2012).
- [4] Y. Xie, B. I. Popa, L. Zigoneanu, and S. A. Cummer, Measurement of a broadband negative index with space-coiling acoustic metamaterials, *Phys. Rev. Lett.* **110**, 175501 (2013).
- [5] N. Kaina, F. Lemoult, M. Fink, and G. Lerosey, Negative refractive index and acoustic superlens from multiple scattering in single negative metamaterials, *Nature (London)* **525**, 77 (2015).
- [6] S. A. Cummer, B.-I. Popa, D. Schurig, D. R. Smith, J. Pendry, M. Rahm, and A. Starr, Scattering theory derivation of a 3D acoustic cloaking shell, *Phys. Rev. Lett.* **100**, 024301 (2008).
- [7] L. Zigoneanu, B. I. Popa, and S. A. Cummer, Three-dimensional broadband omnidirectional acoustic ground cloak, *Nat. Mater.* **13**, 352 (2014).
- [8] C. Faure, O. Richoux, S. Flix, and V. Pagneux, Experiments on metasurface carpet cloaking for audible acoustics, *Appl. Phys. Lett.* **108**, 064103 (2016).
- [9] B. Liang, X. S. Guo, J. Tu, D. Zhang, and J. C. Cheng, An acoustic rectifier, *Nat. Mater.* **9**, 989 (2010).
- [10] R. Fleury, D. L. Sounas, C. F. Sieck, M. R. Haberman, and A. Alù, Sound isolation and giant linear nonreciprocity in a compact acoustic circulator, *Science* **343**, 516 (2014).
- [11] H. Nguyen, Q. Wu, X. Xu, H. Chen, S. Tracy, and G. Huang, Broadband acoustic silencer with ventilation based on slit-type Helmholtz resonators, *Appl. Phys. Lett.* **117**, 134103 (2020).
- [12] Z. Su, Y. Zhu, S. Gao, H. Luo, and H. Zhang, High-efficient and broadband acoustic insulation in a ventilated channel with acoustic metamaterials, *Mech. Eng.* **8**, 857788 (2022).
- [13] Z. Xiao, P. Gao, X. He, Y. Qu, and L. Wu, Multifunctional acoustic metamaterial for air ventilation, broadband sound insulation and switchable transmission, *J. Phys. D: Appl. Phys.* **56**, 044006 (2022).
- [14] X. Xiang, X. Wu, X. Li, P. Wu, H. He, Q. Mu, S. Wang, Y. Huang, and W. Wen, Ultra-open ventilated metamaterial absorbers for sound-silencing applications in environment with free air flows, *Extreme Mech. Lett.* **39**, 100786 (2020).
- [15] S. Kumar and H. P. Lee, Labyrinthine acoustic metastructures enabling broadband sound absorption and ventilation, *Appl. Phys. Lett.* **116**, 134103 (2020).
- [16] L. J. Li, B. Zheng, L. M. Zhong, J. Yang, B. Liang, and J. C. Cheng, Broadband compact acoustic absorber with high efficiency ventilation performance, *Appl. Phys. Lett.* **113**, 103501 (2018).
- [17] Z. X. Xu, H. Gao, Y. J. Ding, J. Yang, B. Liang, and J. C. Cheng, Topology-optimized omnidirectional broadband acoustic ventilation barrier, *Phys. Rev. Appl.* **14**, 054016 (2020).
- [18] J. Mei, G. Ma, M. Yang, Z. Yang, W. Wen, and P. Sheng, Dark acoustic metamaterials as super absorbers for low-frequency sound, *Nat. Commun.* **3**, 756 (2012).
- [19] G. Ma, M. Yang, S. Xiao, Z. Yang, and P. Sheng, Acoustic metasurface with hybrid resonances, *Nat. Mater.* **13**, 873 (2014).
- [20] X. Cai, Q. Guo, G. Hu, and J. Yang, Ultrathin low-frequency sound absorbing panels based on coplanar spiral tubes or coplanar Helmholtz resonators, *Appl. Phys. Lett.* **105**, 121901 (2014).
- [21] M. Yang, G. Ma, Z. Yang, and P. Sheng, Subwavelength perfect acoustic absorption in membrane-type metamaterials: A geometric perspective, *C. R. Mec.* **343**, 635 (2015).
- [22] M. Yang, C. Meng, C. Fu, Y. Li, Z. Yang, and P. Sheng, Subwavelength total acoustic absorption with degenerate resonators, *Appl. Phys. Lett.* **107**, 104104 (2015).
- [23] Y. Li and B. M. Assouar, Acoustic metasurface-based perfect absorber with deep subwavelength thickness, *Appl. Phys. Lett.* **108**, 063502 (2016).
- [24] X. Wu, C. Fu, X. Li, Y. Meng, Y. Gao, J. Tian, L. Wang, Y. Huang, Z. Yang, and W. Wen, Low-frequency tunable acoustic absorber based on split tube resonators, *Appl. Phys. Lett.* **109**, 043501 (2016).
- [25] C. Fu, X. Zhang, M. Yang, S. Xiao, and Z. Yang, Hybrid membrane resonators for multiple frequency asymmetric absorption and reflection in large waveguide, *Appl. Phys. Lett.* **110**, 021901 (2017).

- [26] M. Yang, S. Chen, C. Fu, and P. Sheng, Optimal sound-absorbing structures, *Mater. Horiz.* **4**, 673 (2017).
- [27] Z. Zhou, S. Huang, D. Li, J. Zhu, and Y. Li, Broadband impedance modulation via non-local acoustic metamaterials, *Natl. Sci. Rev.* **9**, nwab171 (2022).
- [28] V. Romero-García, N. Jiménez, J.-P. Groby, A. Merkel, V. Tournat, G. Theocharis, O. Richoux, and V. Pagneux, Perfect absorption in mirror-symmetric acoustic metascreens, *Phys. Rev. Appl.* **14**, 054055 (2020).
- [29] Y. Meng, V. Romero-García, G. Gabard, J.-P. Groby, C. Bricault, and S. Goudé, Subwavelength broadband perfect absorption for unidimensional open-duct problems, *Adv. Mater. Technol.* **8**, 2201909 (2023).
- [30] Y. Meng, V. Romero-García, G. Gabard, J.-P. Groby, C. Bricault, S. Goudé, and P. Sheng, Fundamental constraints on broadband passive acoustic treatments in unidimensional scattering problems, *Proc. R. Soc. A* **478**, 20220287 (2022).
- [31] J. Boulvert, G. Gabard, V. Romero-García, and J.-P. Groby, Compact resonant systems for perfect and broadband sound absorption in wide waveguides in transmission problems, *Sci. Rep.* **12**, 10013 (2022).
- [32] Y. D. Chong, L. Ge, H. Cao, and A. D. Stone, Coherent perfect absorbers: Time-reversed lasers, *Phys. Rev. Lett.* **105**, 053901 (2010).
- [33] W. Wan, Y. Chong, L. Ge, H. Noh, A. D. Stone, and H. Cao, Time-reversed lasing and interferometric control of absorption, *Science* **331**, 889 (2011).
- [34] J. Zhang, K. F. MacDonald, and N. I. Zheludev, Controlling light-with-light without nonlinearity, *Light Sci. Appl.* **1**, e18 (2012).
- [35] D. G. Baranov, A. Krasnok, T. Shegai, A. Alù, and Y. Chong, Coherent perfect absorbers: Linear control of light with light, *Nat. Rev. Mater.* **2**, 1 (2017).
- [36] K. Pichler, M. Kühmayer, J. Böhm, A. Brandstötter, P. Ambichl, U. Kuhl, and S. Rotter, Random antilasing through coherent perfect absorption in a disordered medium, *Nature (London)* **567**, 351 (2019).
- [37] C. Wang, W. R. Sweeney, A. D. Stone, and L. Yang, Coherent perfect absorption at an exceptional point, *Science* **373**, 1261 (2021).
- [38] S. Li, J. Luo, S. Anwar, S. Li, W. Lu, Z. H. Hang, Y. Lai, B. Hou, M. Shen, and C. Wang, Broadband perfect absorption of ultrathin conductive films with coherent illumination: Superabsorption of microwave radiation, *Phys. Rev. B* **91**, 220301(R) (2015).
- [39] Y. Li, M. Qi, J. Li, P. C. Cao, D. Wang, X. F. Zhu, C.-W. Qiu, and H. Chen, Heat transfer control using a thermal analogue of coherent perfect absorption, *Nat. Commun.* **13**, 2683 (2022).
- [40] J. Z. Song, P. Bai, Z. H. Hang, and Y. Lai, Acoustic coherent perfect absorbers, *New. J. Phys.* **16**, 033026 (2014).
- [41] P. Wei, C. Croënne, S. Tak Chu, and J. Li, Symmetrical and anti-symmetrical coherent perfect absorption for acoustic waves, *Appl. Phys. Lett.* **104**, 121902 (2014).
- [42] Y. Duan, J. Luo, G. Wang, Z. H. Hang, B. Hou, J. Li, P. Sheng, and Y. Lai, Theoretical requirements for broadband perfect absorption of acoustic waves by ultra-thin elastic meta-films, *Sci. Rep.* **5**, 12139 (2015).
- [43] C. Meng, X. Zhang, S. T. Tang, M. Yang, and Z. Yang, Acoustic coherent perfect absorbers as sensitive null detectors, *Sci. Rep.* **7**, 43574 (2017).
- [44] M. Lanoy, R.-M. Guillermic, A. Strybulevych, and J. H. Page, Broadband coherent perfect absorption of acoustic waves with bubble metascreens, *Appl. Phys. Lett.* **113**, 171907 (2018).
- [45] M. Farooqui, Y. Aurégan, and V. Pagneux, Ultrathin resistive sheets for broadband coherent absorption and symmetrization of acoustic waves, *Phys. Rev. Appl.* **18**, 014007 (2022).
- [46] M. L. Munjal, *Acoustics of Ducts and Mufflers with Application to Exhaust and Ventilation System Design* (Wiley, New York, 1987).
- [47] See Supplemental Material at <http://link.aps.org/supplemental/10.1103/PhysRevResearch.5.L042020> for details on (1) detailed derivations for obtaining the minimal volume requirement of side-loaded absorbers from the causality principle, (2) correction of target surface impedance arising from higher-order resonances, and (3) the detailed methodology for designing BACPA.
- [48] M. A. Dodd, US Patent No. 9,191,747 (17 November, 2015).
- [49] J. A. Oclee-Brown and C. Spear, US Patent No. 11,490,210 (1 November, 2022).